Self-consistent tensor network method for correlated super-moiré matter beyond one billion sites

Yitao Sun,* Marcel Niedermeier, Tiago V. C. Antão, Adolfo O. Fumega, and Jose L. Lado
Department of Applied Physics, Aalto University, 02150 Espoo, Finland

(Received 13 March 2025; accepted 8 November 2025; published 12 December 2025)

Moiré and super-moiré materials provide exceptional platforms to engineer exotic correlated quantum matter. The vast number of sites required to model moiré systems in real space remains a formidable challenge due to the immense computational resources required. Super-moiré materials push this requirement to the limit, where millions or even billions of sites need to be considered, a requirement beyond the capabilities of conventional methods for interacting systems. Here, we establish a methodology that allows solving correlated states in systems reaching a billion sites, which exploits tensor network representations of real-space Hamiltonians and self-consistent real-space mean-field equations. Our method combines a tensor network kernel polynomial method with quantics tensor cross-interpolation algorithm, enabling us to solve ultralarge models, including those whose single-particle Hamiltonian is too large to be stored explicitly. We demonstrate our methodology with super-moiré systems featuring spatially modulated hoppings, many-body interactions, and domain walls, showing that it allows access to self-consistent symmetry-broken states and spectral functions of real-space models reaching a billion sites. Our methodology provides a strategy to solve exceptionally large interacting problems, providing a widely applicable strategy to compute correlated super-moiré quantum matter.

DOI: 10.1103/krjp-mn4v

I. INTRODUCTION

Twisted moiré materials have enabled creating of a wide variety of correlated states of matter, including unconventional superconducting phases [1–6], topological states [7–10], and correlated insulators [11–14]. These emergent states stem from the moiré pattern between twisted or mismatched 2D materials [15], ideas that have been extended to a variety of artificial platforms including optical metamaterials [16–22] and cold atom systems [23–26]. The moiré pattern gives rise to an emergent periodicity and associated unit cells ranging from thousands to hundreds of thousands of sites, reaching the limits of theoretical atomistic methods to study correlated phases [27–32]. When two or more moiré patterns coexist, a super-moiré pattern emerges, leading to an even wider variety of exotic phases [33,34]. However, super-moiré materials require treating systems from millions to hundreds of millions of sites, which is a challenge for conventional computational methods.

In many-body physics, tensor network algorithms have provided an exceptional method to treat systems with ultralarge many-body Hilbert spaces [35–38]. The essence of tensor networks is to compress a Hilbert space of dimension 2^L with a linearly scaling variational product of tensors. This strategy has provided the most accurate solutions to paradigmatic quantum many-body problems [39–42], and has been recently extended to tackle problems in machine learning [43–45], quantum computing [46–48], and ultimately general problems that require dealing with ultralarge structures of data and integrals [49–58]. Therefore, the capability of tensor networks to deal with ultralarge systems may provide a way forward to tackle problems of interacting super-moiré materials [59].

Here, we establish a tensor network methodology to solve correlated states in super-moiré systems reaching a billion sites. Our method uses an atomistic self-consistent mean-field approach where both single-particle and interacting mean-field terms are expressed purely as tensor networks, using a combination of tensor network Chebyshev expansions and quantics tensor cross-interpolation (QTCI). Our strategy leverages a mapping between the mean-field Hamiltonian of an exponentially large super-moiré system to a linearly scaling pseudospin many-body problem. This methodology allows for the treatment of super-moiré systems whose mean-field Hamiltonian is too large to be explicitly stored, enabling us to deal with system sizes beyond the capabilities of techniques with sparse matrix representations. We demonstrate our method in several super-moiré structures with over one billion atomic sites, showing that it allows us to solve self-consistently interacting problems with spatially varying hoppings and interactions. This work thus provides a methodology capable of dealing with the exceptional system sizes required for correlated phases in super-moiré quantum matter. The paper is organized as follows. In Sec. II, we briefly introduce the mean-field algorithm employed in this work. Section III illustrates the construction of the tensor network representation of the tight-binding Hamiltonian using the hopping Hamiltonian of a one-dimensional model as an example.

*Contact author: yitao.sun@aalto.fi

Published by the American Physical Society under the terms of the Creative Commons Attribution 4.0 International license. Further distribution of this work must maintain attribution to the author(s) and the published article's title, journal citation, and DOI.

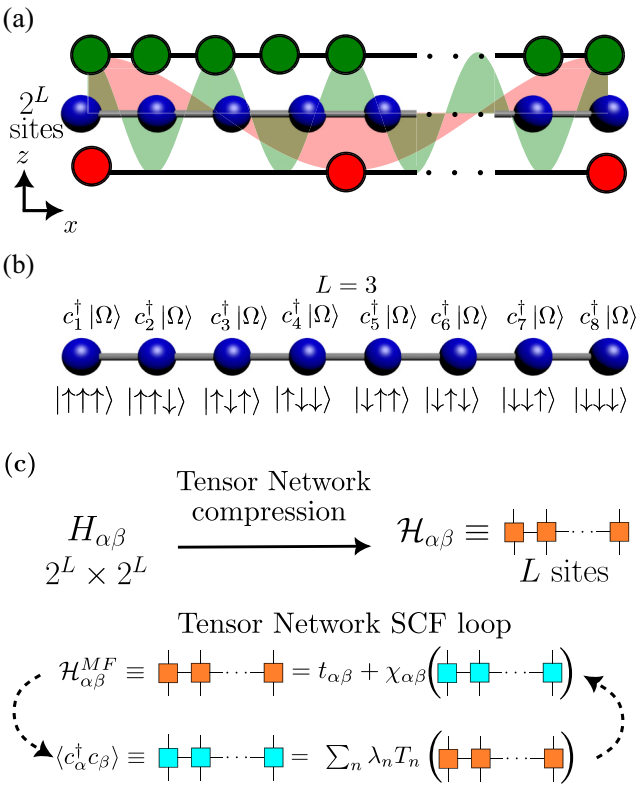


FIG. 1. Schematic of the tensor network self-consistent algorithm for super-moiré matter. Panel (a) shows a schematic of a system featuring two moiré patterns due to the mismatch of top and bottom substrates. Panel (b) shows an example of representing electron states in fermionic and pseudospin bases. Panel (c) shows the tensor network compression and mean-field algorithm, where the fermionic problem is mapped to a pseudospin problem.

The numerical results for mean-field calculations over various one- and two-dimensional super-moiré systems are presented in Sec. IV, together with a discussion of the advantages and possible extensions of our methodology. Finally, Sec. V summarizes the main findings of this study.

II. SELF-CONSISTENT TENSOR NETWORK ALGORITHM

We consider a generic interacting real-space Hamiltonian of a super-moiré system with $N = 2^L$ sites as shown in Fig. 1(a), which has both single-particle and density-density many-body interactions taking the form

$$H = H_0 + H_V = \sum_{\alpha\beta} t_{\alpha\beta} c_\alpha^\dagger c_\beta + \sum_{\alpha\beta} V_{\alpha\beta} c_\alpha^\dagger c_\alpha c_\beta^\dagger c_\beta, \qquad (1)$$

where $t_{\alpha\beta}$ are single-particle hopping amplitudes in the system and $V_{\alpha\beta}$ account for the many-body density-density interactions. The previous Hamiltonian can be solved at the mean-field level by performing the mean-field decoupling $H_V \approx H_V^{\rm MF}$ where $H_V^{\rm MF} = \sum_{\alpha\beta} V_{\alpha\beta}\langle c_\alpha^\dagger c_\alpha\rangle c_\beta^\dagger c_\beta + \cdots = \sum_{\alpha\beta} \chi_{\alpha\beta} c_\alpha^\dagger c_\beta$, "$\cdots$" denoting the remaining Wick contractions. This decoupling gives rise to a mean-field Hamiltonian of the form

$$H^{\rm MF} = \sum_{\alpha\beta} (t_{\alpha\beta} + \chi_{\alpha\beta}) c_\alpha^\dagger c_\beta = \sum_{\alpha\beta} H^{\rm MF}_{\alpha\beta} c_\alpha^\dagger c_\beta, \qquad (2)$$

with $H^{\rm MF}_{\alpha\beta} \equiv H^{\rm MF}_{\alpha\beta}[V_{\alpha\beta}, \langle c_\alpha^\dagger c_\beta\rangle]$ parametrizing the self-consistent mean-field Hamiltonian including single-particle and many-body corrections. For large systems beyond millions of sites, the mean-field Hamiltonian $H^{\rm MF}$ becomes too large to be even stored. We can now reinterpret the 2^L-site mean-field Hamiltonian as a many-body operator of an auxiliary many-body pseudospin chain of L sites, for which the index α, β corresponds to an element of the pseudospin many-body basis as $\alpha \equiv (s_1, s_2, \ldots, s_L)$ and $\beta \equiv (s_1', s_2', \ldots, s_L')$. In this form, the mean-field Hamiltonian can be written using a tensor network representation as a matrix product operator (MPO) in the pseudospin basis as

$$\mathcal{H}^{\rm MF}_{\alpha\beta} \equiv \Gamma^{(1)}_{s_1,s_1'} \Gamma^{(2)}_{s_2,s_2'} \Gamma^{(3)}_{s_3,s_3'} \cdots \Gamma^{(L)}_{s_L,s_L'}, \qquad (3)$$

where $\Gamma^{(n)}_{s_1,s_1'}$ are tensors of dimension m, the bond dimension of the MPO. The structured nature of a super-moiré Hamiltonian enables the representation of $H^{\rm MF}_{\alpha\beta}$ with a manageable bond dimension [49,50]. The main problem to solve the interacting system is then to find the tensor network representation $\mathcal{H}^{\rm MF}$ of $H^{\rm MF}$ in Eq. (2), which can be done by solving a Chebyshev tensor network self-consistent equation [60–65]. The essential objects to compute are correlators $\langle c_\alpha^\dagger c_\beta\rangle = \int_{-\infty}^{\epsilon_F} \langle\alpha|\delta(\omega - \mathcal{H}^{\rm MF})|\beta\rangle d\omega$, with the matrix product state (MPS) $|\alpha\rangle = c_\alpha^\dagger|\Omega\rangle$ as shown in Fig. 1(b), $|\Omega\rangle$ the vacuum state, ϵ_F the Fermi energy, and $\delta(\omega - \mathcal{H}^{\rm MF})$ the Dirac delta function operator. We can now compute all the expectation values as

$$\langle c_\alpha^\dagger c_\beta\rangle = \langle\alpha|\Xi(\mathcal{H}^{\rm MF})|\beta\rangle, \qquad (4)$$

where $\Xi(\mathcal{H}^{\rm MF})$ is the tensor network representation of the density matrix computed with a tensor network Chebyshev kernel polynomial method (KPM) [66–70]. By rescaling the bandwidth of $\mathcal{H}^{\rm MF}$ to the interval $(-1, 1)$, the density matrix takes the form

$$\Xi(\mathcal{H}^{\rm MF}) = \sum_n \lambda_n T_n(\mathcal{H}^{\rm MF}), \qquad (5)$$

where $T_n(x)$ are the Chebyshev polynomials with recursion relation $T_n(x) = 2xT_{n-1}(x) - T_{n-2}(x)$ with $T_0 = 1$ and $T_1(x) = x$ [71]. The expansion coefficients are $\lambda_n = \int_{-1}^{\epsilon_F} \frac{2T_n(\omega)}{\pi\sqrt{1-\omega^2}} d\omega$ for $n \geqslant 1$ and $\lambda_0 = \int_{-1}^{\epsilon_F} \frac{T_0(\omega)}{\pi\sqrt{1-\omega^2}} d\omega$. These Chebyshev recursion relations allow us to find a tensor network representation of Eq. (5) by performing sums and contractions between MPOs. While Eq. (5) is not of practical use with large sparse matrix representations, it can be directly applied with MPOs [72].

The previous Chebyshev expansion gives access to all the correlators $\langle c_\alpha^\dagger c_\beta\rangle$. The mean-field decoupling allows us to define a mean-field Hamiltonian from the tensor network representation of the correlators combining Eqs. (4), (5), (2) as shown in Fig. 1(c). Once the self-consistent mean-field Hamiltonian has been obtained, the spatially dependent spectral function $D(\omega, \alpha) = \langle\alpha|\delta(\omega - \mathcal{H}^{\rm MF})|\alpha\rangle$ of the interacting problem can be computed using a tensor network Chebyshev

expansion as

$$D(\omega,\alpha)=\langle\alpha|\left[\sum_n T_n(\mathcal{H}^{\mathrm{MF}})P_n(\omega)\right]|\alpha\rangle, \tag{6}$$

where $P_n(\omega)=\frac{2T_n(\omega)}{\pi\sqrt{1-\omega^2}}$ for $n\geqslant 1$ and $P_0(\omega)=\frac{T_0(\omega)}{\pi\sqrt{1-\omega^2}}$.

III. TENSOR NETWORK REPRESENTATION OF THE SUPER-MOIRÉ MEAN-FIELD HAMILTONIANS

We now elaborate on the explicit form of the MPO representation of the single-particle Hamiltonian H_0 with more details provided in the Appendixes. We first focus on the example of a one-dimensional spinful Fermi-Hubbard system, which has a Hamiltonian

$$H=\sum_{\alpha,s}t_{\alpha,\alpha+1}c^\dagger_{x_{\alpha+1},s}c_{x_\alpha,s}+\mathrm{H.c.}$$
$$+\sum_\alpha U_\alpha\left(c^\dagger_{x_\alpha,\uparrow}c_{x_\alpha,\uparrow}-\frac{1}{2}\right)\left(c^\dagger_{x_\alpha,\downarrow}c_{x_\alpha,\downarrow}-\frac{1}{2}\right), \tag{7}$$

where $t_{\alpha,\alpha+1}$ captures the spatially varying hopping amplitude between two adjacent atomic sites x_α and $x_{\alpha+1}$, and U_α is the Hubbard interaction induced by the super-moiré correlation in a 1D moiré superlattice. We start with a 1D nearest-neighbor hopping $H_{0,\mathrm{NN}}=\sum_{\alpha,s}^{N-1}t(c^\dagger_{x_{\alpha+1},s}c_{x_\alpha,s}+\mathrm{H.c.})$. The MPO representation of the uniform $\mathcal{H}_{0,\mathrm{NN}}$ hopping term could be built from $\mathcal{H}_{0,\mathrm{NN}}=\sum_{l,s}^{L}t(\sigma^+_{l,s}\bigotimes_{m>l}\sigma^-_{m,s}+\mathrm{H.c.})$, where $\sigma^\pm=\frac{1}{2}(\sigma^x\pm i\sigma^y)$, σ^x and σ^y being Pauli matrices, and l and m are the site indices of the L-site MPO $\mathcal{H}_{0,\mathrm{NN}}$. We then address the case of a spatially modulated hopping amplitude $t_{\alpha,\alpha+1}=t(X_\alpha)$, where $X_\alpha=\frac{x_\alpha+x_{\alpha+1}}{2}$. Viewing $t(X_\alpha)$ as a function of X_α, by applying the QTCI algorithm [49,73,74] over $t(X_\alpha)$, we now generate an MPS representation $|\tau\rangle=\sum M^{(1)}_{s_1}M^{(2)}_{s_2}M^{(3)}_{s_3}\cdots M^{(L)}_{s_L}|s_1,s_2,\ldots,s_L\rangle$ storing all $t(X_\alpha)$ values. For each $M^{(j)}_{s_j}$, we introduce an auxiliary index s'_j to obtain a tensor $\Gamma^{(j)}_{s_j,s'_j}$ and enforce a diagonal matrix structure of the data encoded with a contraction of $\Gamma^{(j)}_{s_j,s'_j}\delta_{j,j'}$. Repeating this process for all tensors in $|\tau\rangle$ yields an MPO representation $\mathcal{T}$ that stores a diagonal matrix whose elements are the same as those of $|\tau\rangle$. Eventually, we perform a contraction between $\mathcal{T}$ and $\sum_{l,s}^{L}\sigma^+_{l,s}\bigotimes_{m>l}\sigma^-_{m,s}$, producing an MPO representation of the single-particle Hamiltonian $\mathcal{H}_0=\{[\mathcal{T}\sum_{l,s}^{L}(\sigma^+_{l,s}\bigotimes_{m>l}\sigma^-_{m,s})]+\mathrm{H.c.}\}$. The MPO $\mathcal{H}_0$ faithfully stores the original hopping terms, ensuring $\langle x_\alpha,s|\mathcal{H}_0|x_{\alpha+1},s\rangle\approx t(X_\alpha)$.

IV. RESULTS

A. One-dimensional super-moiré system

We now show results for the one-dimensional model of Eq. (7), with length of $2^{30}(\gtrsim 10^9)$ atomic sites. Such a model can be realized using optical quantum simulation methods [16,75] or in one-dimensional multiwalled nanotubes [76]. We assume $t(X_\alpha)$ to have the form $t(X_\alpha)=1+0.2\cos(k_1X_\alpha)+0.2\cos(k_2X_\alpha)$, where we set $k_1=\frac{2\pi}{5\sqrt{2}}$ and $k_2=\frac{8\pi}{2^{29}\sqrt{3}}$. These correspond to two different moiré scales as shown in Figs. 2(a) and 2(b), which are incommensurate with each other throughout the system.

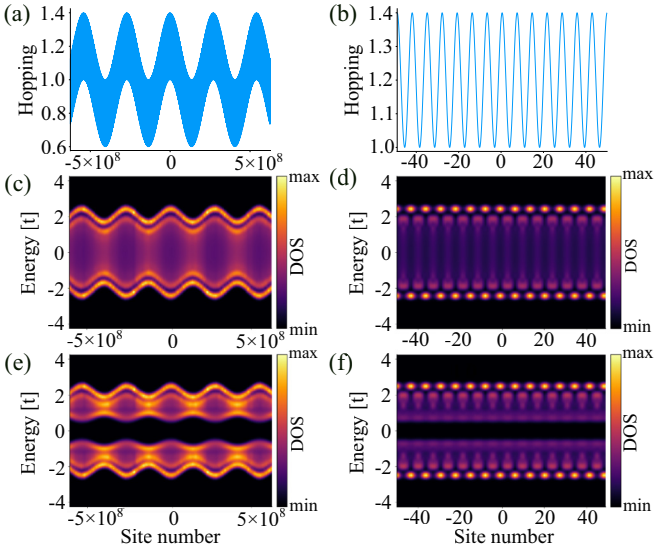


FIG. 2. One-dimensional super-moiré. The super-moiré modulation is included in the hopping amplitudes. Panels (a) and (b) show $t(X_\alpha)$ at the larger moiré scale and smaller moiré scale. Panels (c) and (d) show the corresponding local spectral functions calculated for a system with 2^{30} sites without Hubbard interaction at two different moiré scales. Panels (e) and (f) show the corresponding local spectral functions calculated for a system with Hubbard interaction $U=2.7$ at two different moiré scales.

The local spectral functions for systems with and without Hubbard interaction are shown in Figs. 2(c)–2(f). This tensor network calculation featuring $2^{30}\gtrsim 10^9$ sites required a computational time of 4×10^4 s on a single core of an Intel i5 CPU, leading to a speedup of around four orders of magnitude compared to the estimated run-time that would be required by a previous sparse-matrix-based approach [59], which is in practice infeasible for the system sizes considered here. The interacting solution shows modulations of the spectral function following the larger moiré scale corresponding to k_2 and the smaller moiré scale corresponding to k_1. In the presence of Hubbard on-site interactions, a spatially inhomogeneous gap emerges across the system, which exhibits spatial variations governed by the larger moiré scale yet remains nearly uniform at the smaller moiré scale. This is due to the fact that the scale of the Hubbard interaction considered in this setup is of the same order as the smaller moiré scale, while being negligible in comparison to the larger moiré scale. Consequently, a uniform gap opens across all sites at the smaller moiré scale while being explicitly modulated by the super-moiré correlation at the larger moiré scale.

Next we use the same form of Hamiltonian as in Eq. (7) but include a domain wall by modulating the larger moiré scale k_2 as

$$\tilde{k}_2=k_2\left[1+\delta\tanh\left(\frac{X_\alpha}{W}\right)\right], \tag{8}$$

where δ is a parameter used to quantify the mismatch between the two larger moiré scales separated by the domain wall, and W is the width of the domain wall. We set $\delta=0.2$,

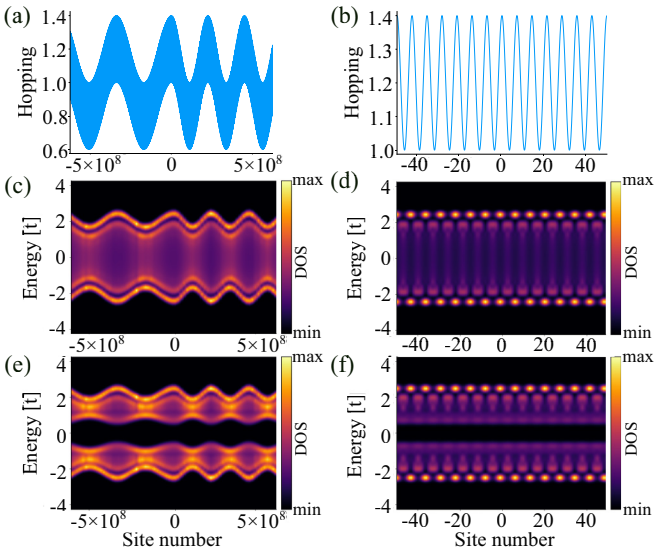


FIG. 3. Domain wall in a one-dimensional super-moiré. The super-moiré modulation is included in the hopping amplitudes, with a domain wall in the middle of the system. Panels (a) and (b) show the hopping amplitudes $t(X_\alpha)$ with the domain wall and two different larger moiré scales and smaller moiré scales. Panels (c) and (d) show the corresponding local spectral functions calculated for a system with $2^{30} \gtrsim 10^9$ sites without Hubbard interaction at two different é scales. Panels (e) and (f) show the corresponding local spectral functions calculated for a system with Hubbard interaction $U = 2.7$ at two different moiré scales.

$W = \frac{2^{30}}{40}$, and keep other parameters consistent with the calculation without the presence of the domain wall. In Figs. 3(c) and 3(e), it is clear that the local spectral functions closely follow the modulation of larger moiré scale on both sides of the domain wall. The opening of the gap due to the Hubbard interaction shown in Fig. 3(e) also obeys this modulation, while at the smaller moiré scale, spectral functions are not influenced by the domain wall as shown in Figs. 3(d) and 3(f).

B. Two-dimensional super-moiré system

To demonstrate the capability of our methodology in handling two-dimensional super-moiré systems, we first conduct mean-field calculations for super-moiré graphene, a platform that has shown great potential in recent experiments [77,78]. We account for the super-moiré modulation of hopping amplitudes in systems both with and without domain walls. In all cases, the Hubbard interaction is fixed at $U = 5.5t$. We consider systems with 2^{31} sites, which have the shape of 2^{16} sites times 2^{15} sites for better visualization of the results. For the case with super-moiré modulation, the hopping amplitudes take the form

$$t_{ij} = 1 + 0.2\sin(k_1\mathbf{u}_{ij}\cdot\mathbf{R}_{ij}) + 0.2\sin(k_2\mathbf{u}_{ij}\cdot\mathbf{R}_{ij}), \quad (9)$$

with $k_1 = \frac{\pi}{2^{12}\sqrt{3}}$ and $k_2 = \frac{\pi}{4\sqrt{2}}$, $\mathbf{u}_{ij}$ one of the three honeycomb bond vectors that point in the same direction as the vector linking sites i and j, and $\mathbf{R}_{ij} = \frac{\mathbf{r}_i+\mathbf{r}_j}{2}$, $\mathbf{r}_i$ being the average of positions i and j. Figures 4(a) and 4(b) display the modulations on all sites of the systems as $t(\mathbf{r_i}) = \sum_j t_{ij}$.

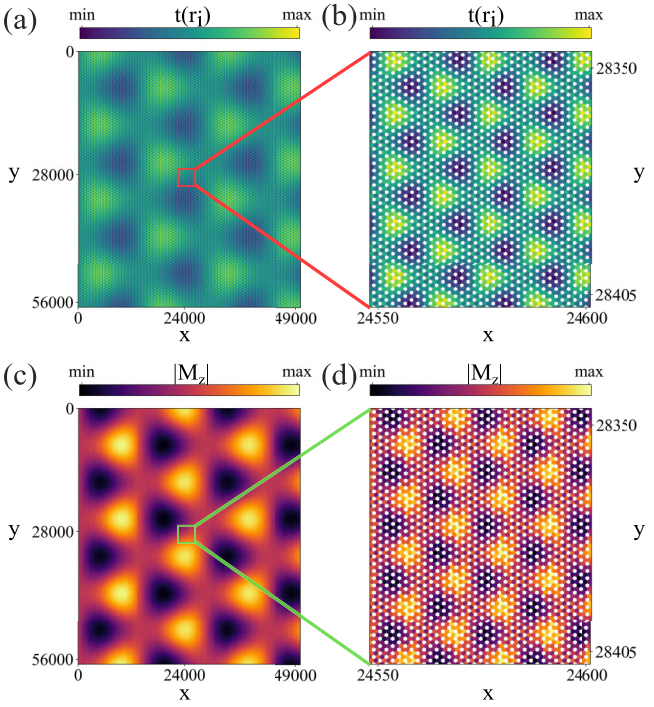


FIG. 4. Two-dimensional honeycomb super-moiré. Results for 2^{31}-site super-moiré modulated honeycomb lattice. Panels (a) and (b) show the super-moiré modulations on the whole system and a center region of the system. Panels (c) and (d) show the magnetization distribution acquired from mean-field calculations corresponding to different length scales.

Then, we consider the existence of a domain wall in the x direction of the system as shown in Figs. 5(a) and 5(b). In this case, we take the hopping amplitudes as

$$t_{ij} = 1 + 0.2\sin(\tilde{k}_1\mathbf{u}_{ij}\cdot\mathbf{R}_{ij}) + 0.2\sin(k_2\mathbf{u}_{ij}\cdot\mathbf{R}_{ij}), \quad (10)$$

while $\tilde{k}_1$ only depends on $X_{ij} = \frac{x_i+x_j}{2}$,

$$\tilde{k}_1 = k_1\left(1 + \delta\tanh\left(\frac{X_{ij}}{W}\right)\right); \quad (11)$$

here, $\delta = 0.3$ and $W = 3000$. In Figs. 4 and 5, we observe that the magnetization $M_z = |\rho_\uparrow - \rho_\downarrow|$, where ρ is the spin-resolved electron density, accurately reflects the hopping modulations across all scales. This agreement confirms the robustness of our method in resolving the real-space structure of super-moiré patterns in ultralarge systems, and it is able to simultaneously capture super-moiré and domain walls.

Furthermore, our methodology can be applied to systems featuring quasicrystalline structures, and when the modulations are not in the hopping but the electronic interactions. We demonstrate this in a square lattice with a modulated Hubbard interaction with 2^{30} ($2^{15}\times 2^{15}$) sites. Such systems can be realized through Coulomb engineering [79–81]. To demonstrate the capability of our method in handling more complex spatial structures, we introduce a modulation on the Hubbard interaction with approximate eightfold rotational symmetry for simulating a quasicrystalline system [5,82,83] as $U(\mathbf{r_i}) = 8 + 0.5\{\sum_{i=1}^{4}\cos(k_1\mathbf{n}_i\cdot\mathbf{r}_i) + \cos(k_2\mathbf{n}_i\cdot\mathbf{r}_i)\}$, where the set of unit vectors $\mathbf{n}_j$ includes $(1,0)^{\mathrm{T}}$, $(0,1)^{\mathrm{T}}$, $(\frac{\sqrt{2}}{2},\frac{\sqrt{2}}{2})^{\mathrm{T}}$, and

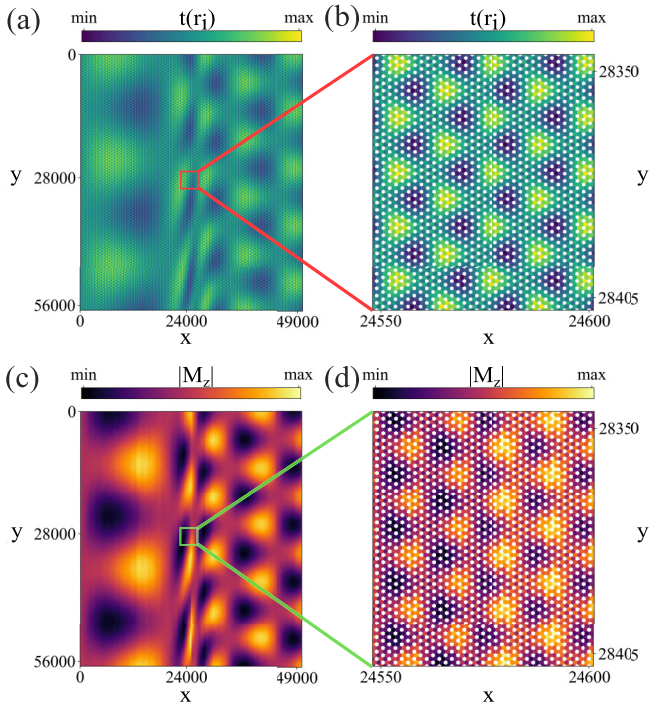


FIG. 5. Domain wall in a two-dimensional honeycomb super-moiré. Results are for 2^{31}-site super-moiré modulated honeycomb lattice with domain wall. Panels (a) and (b) show the super-moiré modulations with domain wall on the whole system and a center region of the system. Panels (c) and (d) show the magnetization distribution acquired from mean-field calculations corresponding to different length scales.

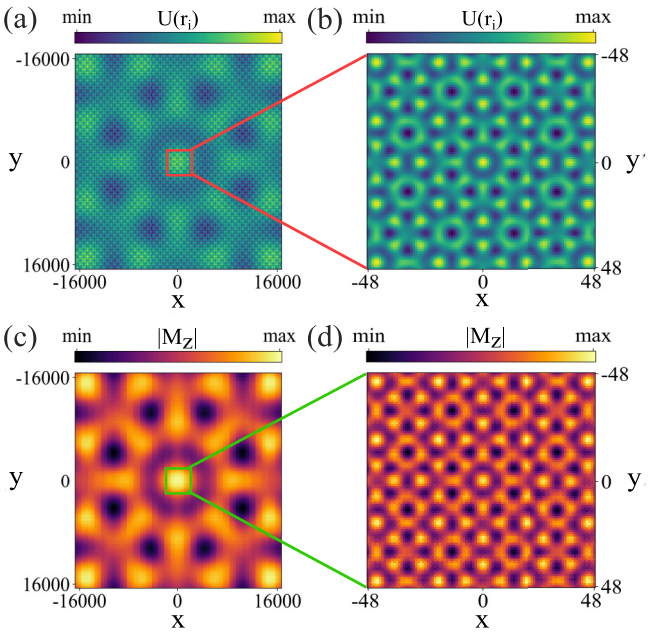


FIG. 6. Two-dimensional eightfold square super-moiré quasicrystal. Results for 2^{30}-site square lattice with super-moiré Hubbard interaction with eightfold rotational symmetry. Panels (a) and (b) show the Hubbard interaction $U(r_i)$ at the larger moiré scale and smaller moiré scale. Panels (c) and (d) show the corresponding magnetization $|M_z|$ calculated for the system at two different moiré scales.

$(-\frac{\sqrt{2}}{2}, \frac{\sqrt{2}}{2})^{\mathrm{T}}$, corresponding to four directions that collectively span an approximate eightfold symmetric basis in two dimensions and $k_1 = \frac{\pi}{2^{11}\sqrt{3}}$, $k_2 = \frac{\pi}{2\sqrt{5}}$. As shown in Figs. 6(a)–6(d), the spatial distribution of local magnetization closely follows the modulation of $U(r_i)$ at both large and small scales. These results confirm that our method accurately captures spatially modulated correlated states and is readily applicable to a wide range of realistic super-moiré and quasicrystalline systems.

A key advantage of our approach is that it bypasses the need to store the single-particle Hamiltonian as sparse matrices like in prior methods [59]. This enables simulations of systems over three orders of magnitude larger. Representing the full Hamiltonian as an MPO also allows KPM calculations without evaluating Chebyshev moments with separate basis vectors, which significantly boosts efficiency. However, this advantage relies on the structured nature of the Hamiltonian in super-moiré systems, where the modulations can be expressed as deterministic functions of spatial coordinates. In contrast, strong randomness in highly disordered systems will significantly hinder the compression of system Hamiltonian via the QTCI algorithm. Furthermore, by encoding the mean-field Hamiltonian as MPOs, our method naturally interfaces with established tensor network algorithms such as real-time evolution [84–88] and can therefore be extended to compute dynamics of super-moiré materials in real space. While our discussion has focused on tight-binding models, it is worth noting that our tensor network mean-field methodology can be readily extended to real-space density functional theory [89–92], which can potentially enable an increase in the system sizes that these methods can reach.

V. CONCLUSION

In summary, we have established a methodology that allows us to solve billion-size interacting super-moiré problems by using a self-consistent tensor network algorithm. Our strategy uses a mapping from the real-space Hamiltonian of a system with a size of 2^L atomic sites into a tensor network representation of a many-body system corresponding to a chain of L-site pseudospins. By using a combination of tensor network Chebyshev expansion and quantics tensor cross-interpolation, we can solve the self-consistent mean-field equations of ultralarge systems. We demonstrate this technique with super-moiré interacting models above a billion sites, featuring a spatially dependent single-particle term and spatially dependent many-body interactions, including domain walls. Our work establishes a widely applicable technique to treat interacting electronic problems, providing a method to solve correlated systems of unprecedented sizes, and in particular whose single-particle Hamiltonian alone is too large to be explicitly stored even with sparse representations. Ultimately, our work provides a starting point to perform many-body perturbation theory and linear response using tensor networks in real space, providing the required method to rationalize a wide range of correlated phenomena in super-moiré quantum matter.

ACKNOWLEDGMENTS

We acknowledge the computational resources provided by the Aalto Science-IT project and the financial support from InstituteQ, the Jane and Aatos Erkko Foundation, the Academy of Finland Projects No. 331342, No. 358088, No. 349696, and No. 369367, Finnish Ministry of Education and Culture through the Quantum Doctoral Education Pilot Program and the Research Council of Finland through the Finnish Quantum Flagship Project No. 358878, and the ERC Consolidator Grant ULTRATWISTROICS (Grant Agreement No. 101170477). We thank X. Waintal, C. Flindt, C. Yu, P. San-Jose, E. Prada, B. Amorim, E. Castro, P. Alcazar, M. Nguyen, and R. Oliveira for useful discussions.

DATA AVAILABILITY

The code used in this work and the data that support the findings of this article are openly available in Ref. [93].

APPENDIX A: CONSTRUCTION OF MATRIX PRODUCT OPERATOR HAMILTONIANS FOR ONE-DIMENSIONAL SYSTEMS

In the following, we elaborate on how we construct the MPOs for the hopping terms used in our 1D and 2D mean-field Hamiltonians. For simplicity, we neglect the electron spin. Starting with the interacting term, assume the Hubbard interaction is a function defined throughout the system as $U(x_i)$; one can directly construct a diagonal MPO $\mathcal{U}$ storing all the function values using the QTCI algorithm [94] with matrix form of

$$\begin{bmatrix} U(x_1) & 0 & 0 & 0 & \cdots & 0 \\ 0 & U(x_2) & 0 & 0 & \cdots & 0 \\ 0 & 0 & U(x_3) & 0 & \cdots & 0 \\ \vdots & \vdots & \vdots & \ddots & \vdots & \vdots \\ 0 & 0 & 0 & \cdots & U(x_{2^L-1}) & 0 \\ 0 & 0 & 0 & \cdots & 0 & U(x_{2^L}) \end{bmatrix}, \tag{A1}$$

where x_i is the spatial position of site i. Then, with the electron density diagonal MPO $\mathcal{N}$ having the matrix form of

$$\begin{bmatrix} n(x_1) & 0 & 0 & 0 & \cdots & 0 \\ 0 & n(x_2) & 0 & 0 & \cdots & 0 \\ 0 & 0 & n(x_3) & 0 & \cdots & 0 \\ \vdots & \vdots & \vdots & \ddots & \vdots & \vdots \\ 0 & 0 & 0 & \cdots & n(x_{2^L-1}) & 0 \\ 0 & 0 & 0 & \cdots & 0 & n(x_{2^L}) \end{bmatrix}, \tag{A2}$$

which is generated in each self-consistent field (SCF) iteration with the QTCI algorithm, the correct on-site interaction term is the contraction $\mathcal{UN}$.

Next, we start with the fundamental ingredient of our construction of all types of hopping Hamiltonians. For the L-site MPO of $\mathcal{S} = \sum_l^L \sigma_l^+ \bigotimes_{m>l} \sigma_m^-$, the matrix form of S will be

$$\begin{bmatrix} 0 & 1 & 0 & 0 & \cdots & 0 \\ 0 & 0 & 1 & 0 & \cdots & 0 \\ 0 & 0 & 0 & 1 & \cdots & 0 \\ 0 & 0 & 0 & 0 & \ddots & 0 \\ \vdots & \vdots & \vdots & \vdots & \ddots & 1 \\ 0 & 0 & 0 & 0 & \cdots & 0 \end{bmatrix}, \tag{A3}$$

with the shape of $2^L \times 2^L$. Then, if the hopping amplitudes of this system are position dependent as shown in the main text, which could be written as a function of spatial coordinate as $t(X)$ where $X_i = \frac{x_i + x_{i+1}}{2}$, one can follow the approach in the paper using the QTCI algorithm and construct a diagonal MPO $\mathcal{T}$ whose matrix form will be

$$\begin{bmatrix} t(X_1) & 0 & 0 & 0 & \cdots & 0 \\ 0 & t(X_2) & 0 & 0 & \cdots & 0 \\ 0 & 0 & t(X_3) & 0 & \cdots & 0 \\ \vdots & \vdots & \vdots & \ddots & \vdots & \vdots \\ 0 & 0 & 0 & \cdots & t(X_{2^L-1}) & 0 \\ 0 & 0 & 0 & \cdots & 0 & t(X_{2^L}) \end{bmatrix}. \tag{A4}$$

For simplicity, here we assume that all functions we have for hopping amplitudes are real. Then, the contraction between $\mathcal{T}$ and $\mathcal{S}$ will result in the matrix

$$\begin{bmatrix} 0 & t(X_1) & 0 & 0 & \cdots & 0 & 0 \\ 0 & 0 & t(X_2) & 0 & \cdots & 0 & 0 \\ 0 & 0 & 0 & t(X_3) & \cdots & 0 & 0 \\ 0 & 0 & 0 & 0 & \ddots & \vdots & \vdots \\ 0 & 0 & 0 & 0 & \ddots & t(X_{2^L-2}) & 0 \\ 0 & 0 & 0 & 0 & 0 & 0 & t(X_{2^L-1}) \\ 0 & 0 & 0 & 0 & 0 & 0 & 0 \end{bmatrix}. \tag{A5}$$

In such a contraction, the $t(X_{2^L})$ term is discarded and all other hopping amplitudes are correctly cast onto $\mathcal{S}$. To construct the other half of the Hamiltonian, one only needs to construct the Hermitian conjugate $(\mathcal{TS})^\dagger$ as

$$\begin{bmatrix} 0 & 0 & 0 & 0 & \cdots & 0 & 0 \\ t(X_1) & 0 & 0 & 0 & \cdots & 0 & 0 \\ 0 & t(X_2) & 0 & 0 & \cdots & 0 & 0 \\ 0 & 0 & t(X_3) & 0 & \cdots & 0 & 0 \\ \vdots & \ddots & \ddots & \ddots & \ddots & \vdots & \vdots \\ 0 & \cdots & \cdots & \cdots & t(X_{2^L-2}) & 0 & 0 \\ 0 & \cdots & \cdots & \cdots & 0 & t(X_{2^L-1}) & 0 \end{bmatrix}. \tag{A6}$$

Summing the two components $\mathcal{TS} + (\mathcal{TS})^\dagger$, we are able to construct the hopping MPO for one-dimensional nearest-neighbor hopping systems. Then, $\mathcal{TS} + (\mathcal{TS})^\dagger + \mathcal{UN}$ will result in the full Hamiltonian expressed in the form of MPO.

It is straightforward to extend this approach to long-range hoppings. For the construction of next-nearest-neighbor hopping MPO, it will simply be the square of $\mathcal{S}$, as the matrix

form of such square of $\mathcal{S}$ is

$$\begin{bmatrix} 0 & 0 & 1 & 0 & \cdots & 0 \\ 0 & 0 & 0 & 1 & \cdots & 0 \\ 0 & 0 & 0 & 0 & \cdots & 0 \\ 0 & 0 & 0 & 0 & \ddots & 1 \\ \vdots & \vdots & \vdots & \vdots & \ddots & 0 \\ 0 & 0 & 0 & 0 & \cdots & 0 \end{bmatrix}, \tag{A7}$$

which shifts the values on first off-diagonal line to second off-diagonal line. Through this approach, we can construct MPOs for shifting matrix elements for even larger distances. For the notations, we call the original $\mathcal{S}$ to be $\mathcal{S}_0$ as it will shift the matrix elements of any MPO it applies on by $2^0 = 1$ line. Such shifting MPOs allow one to easily construct hopping MPOs for large-scale systems with arbitrary long-range hoppings or couplings. For example, to construct the shifting MPO $\mathcal{S}_{2^N}$, where N is an arbitrary integer, one simply needs to perform

$$\mathcal{S}_{2^N} = \prod_{i=1}^{N} \mathcal{S}_1 = \prod_{i=1}^{N} (\mathcal{S}_0)^2. \tag{A8}$$

This example shown here will be significant for the construction of hopping MPOs for two-dimensional systems. On the other hand, to shift the lines down, one can use the Hermitian conjugate of these shifting MPOs. Eventually, since every decimal number can be expressed with a binary expression, in principle, our approach allows one to shift the diagonal elements to arbitrary positions in the matrix, making it possible to construct the MPO for Hamiltonians with complex structures.

APPENDIX B: CONSTRUCTION OF MATRIX PRODUCT OPERATOR FOR TWO-DIMENSIONAL SYSTEMS

Next, we explain how to construct hopping MPOs for two-dimensional systems. The core idea is to view the 2D lattices as separate 1D chains with intrachain and interchain hoppings as shown in Fig. 7.

We can first consider a square lattice with size of $2^M \times 2^M$. If we assume that intrachain hopping has the direction of x and interchain hopping has the direction of y, we can construct two diagonal MPOs $\mathcal{T}_{\text{intra}}$ and $\mathcal{T}_{\text{inter}}$ with $2M$ sites based on X_i and $Y_i = \frac{y_i + y_{i+1}}{2}$. $\mathcal{T}_{\text{intra}}$ should have the form of $\bigoplus^{2^M} \mathcal{T}_X$, where $\mathcal{T}_X$ has the matrix form of

$$\begin{bmatrix} t(X_1) & 0 & 0 & 0 & \cdots & 0 \\ 0 & t(X_2) & 0 & 0 & \cdots & 0 \\ 0 & 0 & t(X_3) & 0 & \cdots & 0 \\ \vdots & \vdots & \vdots & \ddots & \vdots & \vdots \\ 0 & 0 & 0 & \cdots & t(X_{2^M-1}) & 0 \\ 0 & 0 & 0 & \cdots & 0 & t(X_{2^M}) \end{bmatrix}, \tag{B1}$$

so that this block repeats 2^M times for all the chains in the system. However, $\mathcal{T}_{\text{inter}}$ should have the matrix form of $\bigoplus_{j=1}^{2^M} \mathcal{T}_{Y_j}$, where $\mathcal{T}_{Y_j} = t(Y_j)(\mathcal{I}_{2^M})$, $\mathcal{I}_{2^M}$ being the MPO of identity matrix with shape of $2^M \times 2^M$. In this way, all the hopping amplitudes between two neighboring chains are the same, as shown in Fig. 7(b).

We can then construct the correct hopping MPO using $\mathcal{T}_{\text{intra}}$ and $\mathcal{T}_{\text{inter}}$. First of all, the intrachain hoppings will be very similar as in the 1D cases. One just needs to notice that from the site with index of 2^M to the site with index $2^M + 1$, there is no actual hopping in the 2D cases since this is where the first chain ends and the second chain starts, which is shown in Fig. 7(b). Thus, after the generation of the diagonal MPO $\mathcal{T}_{\text{intra}}$, an additional operator $\mathcal{B}$ will be needed to erase the diagonal values exactly at positions proportional to the length of the chain 2^M. The matrix form of it will be

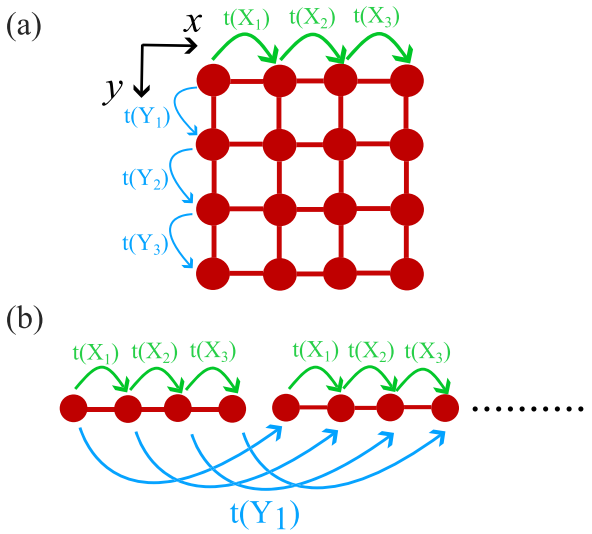


FIG. 7. Schematic of the construction of two-dimensional Hamiltonians. A 16-site square lattice example to show how we map the two-dimensional system to one-dimensional chains with intra and interchain hoppings. Panel (a) shows the original system where we mark the hopping amplitudes in x direction with $t(X_i)$ and in y direction with $t(Y_i)$. Panel (b) demonstrates the equivalent 1D chains showing that the original $t(X_i)$ become intrachain hoppings and $t(Y_i)$ become the interchain hoppings.

$$\bigoplus^{2^M} \begin{bmatrix} \mathbf{I}_{2^M-1} & \mathbf{0}_{1\times(2^M-1)} \\ \mathbf{0}_{(2^M-1)\times 1} & 0 \end{bmatrix}. \tag{B2}$$

This MPO could be constructed from the QTCI algorithm or one can construct it in a pure product of tensor approach as

$$\mathcal{B} = \bigotimes_{i=1}^{2M} \sigma_i^0 - \left(\bigotimes_{i=1}^{2M} \sigma_i^0 \right) \prod_{j=M+1}^{2M} \sigma_j^d, \tag{B3}$$

where σ_i^0 is the identity matrix operator acting on the ith site of tensor network and $\sigma_i^d = \frac{1}{2}(\sigma_i^0 - \sigma_i^z)$. Then, the correct intrachain hopping MPO will be $\mathcal{B}\mathcal{T}_{\text{intra}}\mathcal{S}_0 + \text{H.c.}$, where $\mathcal{B}\mathcal{T}_{\text{intra}}\mathcal{S}_0$ will have the matrix form of

$$\left(\bigoplus^{2^M-1} (T_{\text{shifted}} \oplus 0) \right) \oplus T_{\text{shifted}}, \tag{B4}$$

and T_{shifted} is the matrix of the form

$$\begin{bmatrix} 0 & t(X_1) & 0 & \cdots & 0 & 0 \\ 0 & 0 & t(X_2) & \cdots & 0 & 0 \\ \vdots & \vdots & \ddots & \ddots & \vdots & \vdots \\ 0 & 0 & \cdots & 0 & t(X_{2^M-2}) & 0 \\ 0 & 0 & \cdots & 0 & 0 & t(X_{2^M-1}) \\ 0 & 0 & \cdots & 0 & 0 & 0 \end{bmatrix}. \tag{B5}$$

For the interchain hopping terms, once the diagonal MPO $\mathcal{T}_{\text{inter}}$ is constructed, it can be correctly positioned by shifting it upward by 2^M lines. As illustrated in Fig. 7, the site index difference between two coupled sites in adjacent chains is exactly 2^M, meaning the corresponding off-diagonal terms in the original Hamiltonian appear 2^M lines above the main diagonal. Therefore, shifting $\mathcal{T}_{\text{inter}}$ upward by 2^M aligns it with the correct off-diagonal structure in the full Hamiltonian. As discussed in Appendix A, this only requires a shifting operator $\mathcal{S}_{2^M}$ and could simply be finished with M times of contraction of $\mathcal{S}_1$. Then, the correct MPO for the interchain hopping for square lattice will simply be $\mathcal{T}_{\text{inter}}\mathcal{S}_{2^M} + \text{H.c.}$. Eventually, the correct MPO for the hopping Hamiltonian of square lattice is $\mathcal{B}\mathcal{T}_{\text{intra}}\mathcal{S}_0 + \mathcal{T}_{\text{inter}}\mathcal{S}_{2^M} + \text{H.c.}$

Furthermore, starting from the construction of the hopping MPOs for the square lattice, one can readily extend the approach to triangular and honeycomb lattices with only few modifications. The construction of intrachain hopping MPOs remains identical to that of the square lattice. While the interchain hopping MPOs are more intricate in these lattices, the same underlying strategy applies: construct the appropriate diagonal MPOs for the hopping terms, shift each component to its correct position, and finally assemble the full Hamiltonian in MPO form.

APPENDIX C: GENERAL COMMENTS ON SPECTRAL RESCALING AND HAMILTONIAN COMPRESSIBILITY

Following our explanations for constructing MPOs, we provide here additional discussion to contextualize the scope and robustness of our methodology. Since our approach combines several advanced numerical techniques, we focus on two central aspects: the application of the kernel polynomial method (KPM) over MPOs and the compressibility of the Hamiltonian via the QTCI algorithm.

1. Spectral rescaling of the mean-field Hamiltonian

Performing the calculations with the KPM algorithm requires a spectral rescaling of the Hamiltonian of the system [71]. In several previous works where KPM method is applied to MPO-form Hamiltonians [66–68,95], careful considerations must be paid to the rescaling of the Hamiltonians onto the energy window of $(-1, 1)$. However, a key distinction between our work and prior studies lies in the type of Hamiltonian considered. While the cited references typically focus on quantum many-body Hamiltonians, our method operates on single-electron mean-field Hamiltonians. In effectively single-particle Hamiltonian, as is our mean-field Hamiltonian in MPO form, the bandwidth is size independent even in the presence of mean-field interactions. Specifically, for a one-dimensional modulated system, the bandwidth of the MPO Hamiltonian is approximately $W \approx 4t + U$, whereas for a two-dimensional square or honeycomb lattice it is approximately $W \approx 8t + U$ or $W \approx 6t + U$. As a result, in our manuscript, spectral functions do not have long tails. This key difference greatly simplifies the rescaling step and mitigates the risk of pathological spectral behavior as the system size increases.

In our implementation, we normalize the single-particle Hamiltonian by an overall factor to ensure that its spectrum falls within the $(-1, 1)$ interval required for the Chebyshev expansion. This simple procedure has proven robust in all models considered, including large-scale 1D and 2D supermoiré systems. If the bandwidth is not known in advance, it can be estimated via the density matrix renormalization group method applied to the MPO to obtain the extremal eigenvalues, which define the required scaling window.

2. Compressibility of the Hamiltonian

In the main text, we commented that the "structured" Hamiltonian of super-moiré system makes it possible to compress it as an MPO. The notion of "structured" in our context refers to the property that the modulation in the Hamiltonian (e.g., moiré or super-moiré patterns) can be expressed as a deterministic function of spatial coordinates, even if the system lacks translational invariance. This functional structure is what allows the application of the QTCI algorithm to efficiently build a tensor train storing all function values for further MPO construction. The capability of the QTCI algorithm in approximating physical observables featuring complicated functions has already been proved in various previous works [49,53,54,94]. Specifically, our algorithm relies on the compressibility of the Hamiltonian, which enables finding a tensor network representation with small bond dimension. Quasiperiodic and quasicrystalline systems fall squarely into this category and are naturally compressible.

For highly disordered systems where every single site is independent from every other one, our methodology would not be effective as such Hamiltonian could not be compressed as a tensor network with small bond dimension. In comparison, sparse disorder, including dilute impurities, twist disorder, or domain walls, is compressible, as the profiles for those systems can be deterministically stored and generated with small resources [49]. Specifically, the 1D and 2D domain wall results presented on our revised manuscript belong to this sparse disorder scenario. From the perspective of tensor networks, compressibility is associated with a matrix product state with a low bond dimension, which represents modulations where the entanglement between length scales is not excessively large [49].

APPENDIX D: ADDITIONAL RESULTS FOR TWO-DIMENSIONAL SYSTEMS

Beyond the two-dimensional results shown in Figs. 4–6, we show here analogous results for a super-moiré two-dimensional square lattice. We consider the super-moiré modulation of the hopping amplitudes and for systems with and without domain walls, where the Hubbard interaction is set to be a constant of $U = 5.5t$.

First, we consider super-moiré square lattice with 2^{30} sites ($2^{15} \times 2^{15}$). Such system could be simulated with photonic lattices and twisted materials [3,96]. The hopping amplitudes of the system take the form

$$t_{ij} = 1 + 0.2\sin(k_1\mathbf{u}_{ij}\cdot\mathbf{R}_{ij}) + 0.2\sin(k_2\mathbf{u}_{ij}\cdot\mathbf{R}_{ij}), \quad \text{(D1)}$$

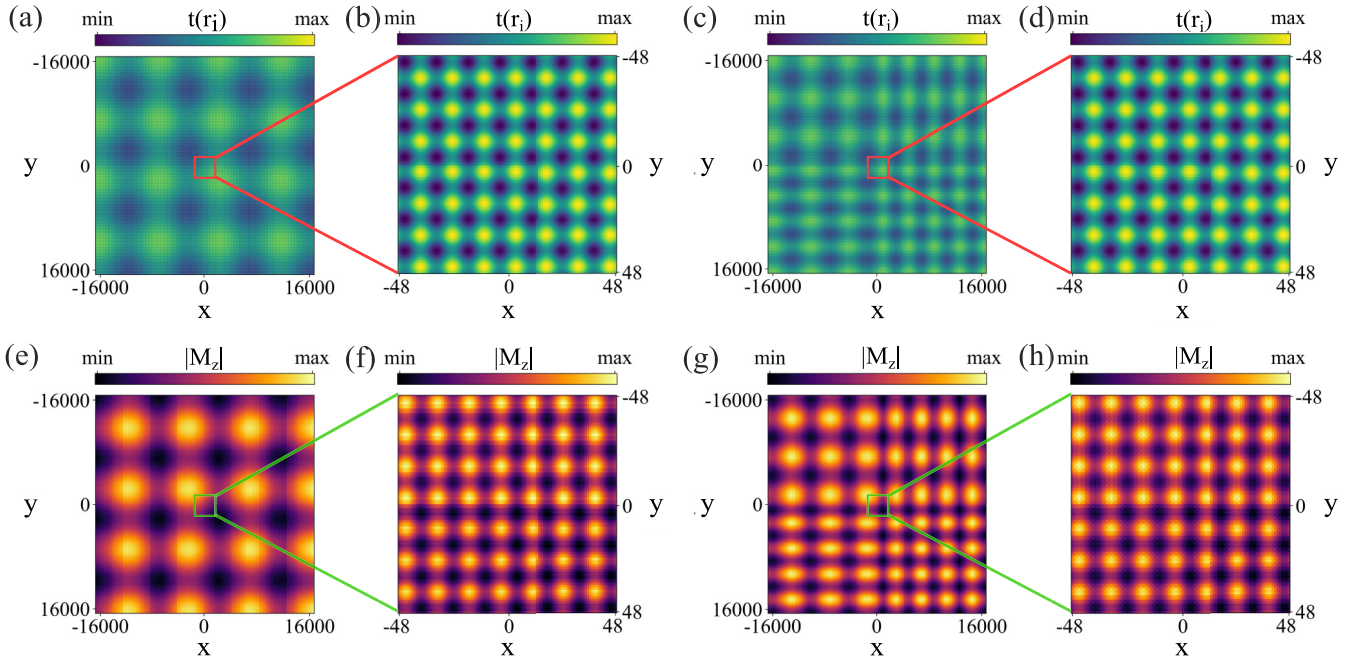


FIG. 8. Two-dimensional square super-moiré lattice. Results for 2^{30}-site super-moiré modulated square lattice with and without domain walls. Panels (a) and (b) show the super-moiré modulations on the whole system and a center region of the system. Panels (c) and (d) show the super-moiré modulations with domain walls on the whole system and a center region of the system. Panels (e)–(h) show the magnetization distribution acquired from mean-field calculations corresponding to different systems and length scales following panels (a)–(d).

where $k_1 = \frac{\pi}{2^{11}\sqrt{5}}$ and $k_2 = \frac{\pi}{4\sqrt{3}}$. $\mathbf{u}_{ij}$ is the vector linking sites i and j, while $\mathbf{R}_{ij} = \frac{\mathbf{r}_i + \mathbf{r}_j}{2}$, $\mathbf{r}_i$ being the average of positions i, j.

We now present the case of domain walls in two dimensions. In this scenario, the hopping modulation associated with the domain wall takes the form

$$t_{ij} = 1 + 0.2\sin(\tilde{k}_1 \mathbf{u}_{ij} \cdot \mathbf{R}_{ij}) + 0.2\sin(k_2 \mathbf{u}_{ij} \cdot \mathbf{R}_{ij}), \quad \text{(D2)}$$

where

$$\tilde{k}_1 = k_1\left(1 + \delta \tanh\left(\frac{\mathbf{u}_{ij} \cdot \mathbf{R}_{ij}}{W}\right)\right). \quad \text{(D3)}$$

The modulation above corresponds to two domain walls in the system in both x and y directions. Here, $\delta = 0.2$ and $W = 819.2$. In Fig. 8, we show the modulations on all sites of the systems $t(\mathbf{r_i}) = \sum_j t_{ij}$ and compare it with the spatial distribution of magnetization obtained from mean-field calculations. In both uniform and domain wall cases, the magnetic textures closely follow the hopping modulation, demonstrating strong spatial correlation at both large and small length scales.

APPENDIX E: PROFILING AND ACCURACY BENCHMARKING

Finally, we profile and benchmark the performance of our methodology using one-dimensional super-moiré systems as in Fig. 9. To demonstrate the increase of efficiency enabled by our methodology, we have computed the time required for solving a self-consistent problem for different system sizes as shown in Fig. 9(a). We vary the system size L and keep the same number of Chebyshev polynomials $N_c = 250$ and bond dimension $\chi = 100$ in all cases. The systems are governed by Hamiltonians of the same form as the systems in Fig. 2, with fixed parameters $k_1 = \frac{2\pi}{5\sqrt{2}}$ and $k_2 = \frac{8\pi}{2^{L-1}\sqrt{3}}$. Calculations are converged to a self-consistency error $\epsilon < 10^{-3}$, where the error in the nth iteration of the mean-field procedure is defined as $\epsilon_n = \max(|\rho_n - \rho_{n-1}|)$.

As shown in Fig. 9(a), the total run-time T for $\mathcal{N} = 10$ rounds of SCF iterations exhibits a linear scaling with an exponential growth in the system size, corresponding to a logarithmic scaling with respect to the total number of lattice sites $N = 2^L$ and the size of the single-particle Hilbert space. For this specific problem and at fixed χ and N_c, our approach achieves $\mathcal{O}(\log N)$ computational complexity, a dramatic improvement over traditional KPM approaches, including our previous sparse-matrix implementation, which typically scale as $\mathcal{O}(N^2)$ [59,71]. We note that this scaling appears from keeping the bond dimension χ and number of Chebyshev polynomials N_c fixed, which in particular enables having a self-consistency error $\epsilon < 10^{-3}$ for all system sizes. In case the parameters χ and N_c were dynamically adjusted to target a specific accuracy, the scaling with the system size may be different. We note that the number of Chebyshev polynomials enforces an effective energy smearing [71], and dynamically updating that may introduce instabilities in the self-consistent loop. The choice of fixing χ and N_c in the self-consistent loop is similar to fixing the maximum kinetic energy of plane waves and the Fermi temperature in density functional theory calculations [97], parameters that are most commonly fixed during the self-consistent loop and are not dynamically updated. It is worth noting that once a solution is converged with

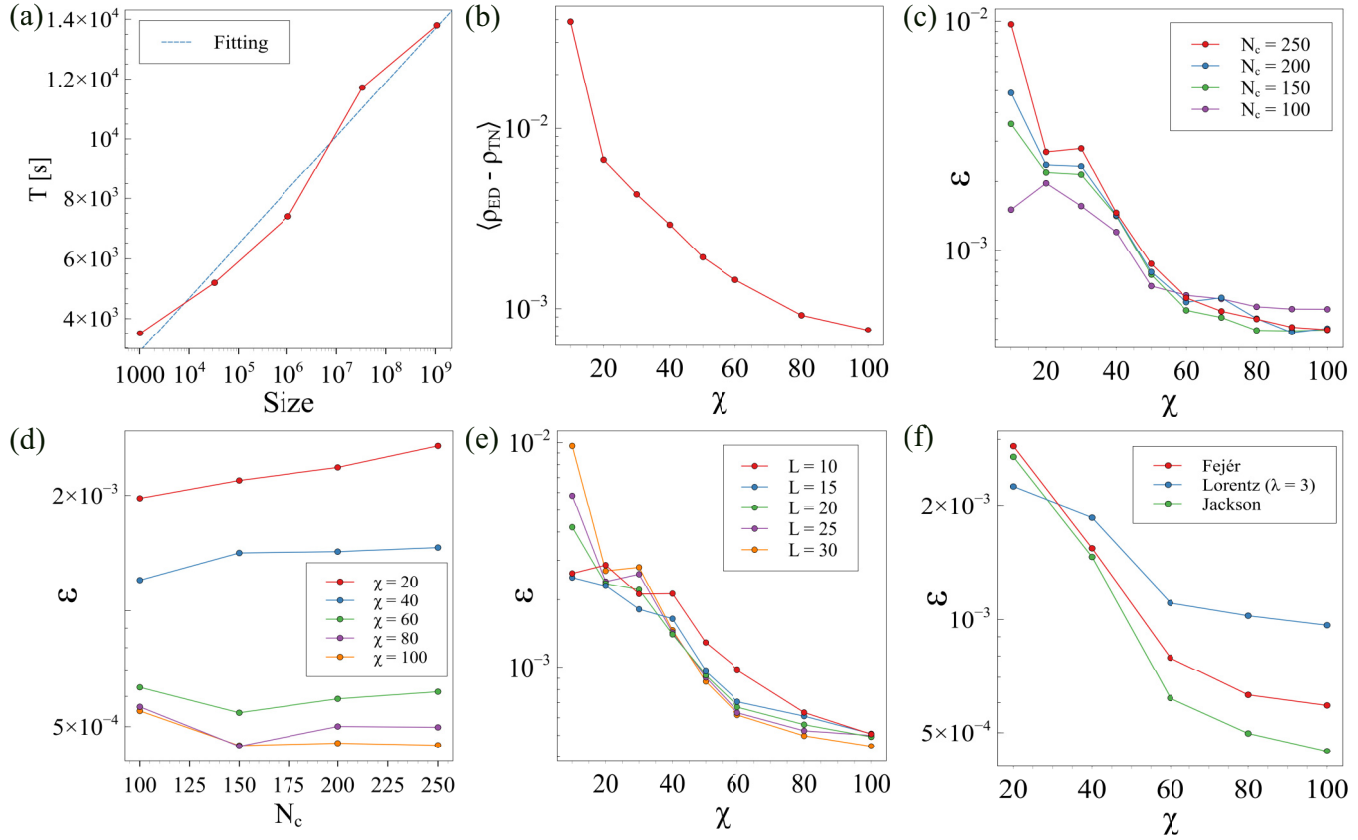


FIG. 9. Profiling and performance benchmarking of the methodology. Panel (a) shows the total computation time for different system sizes along with a linear fit. The calculations are performed on Aalto University's Triton cluster node GPU [49–51] with the GPU Nvidia h200 and the CPU Intel Xeon Platinum 8562Y+. All KPM computations are GPU-accelerated using CUDA [60,64,65]. Panel (b) presents the average deviation between the electron densities obtained from the tensor network approach and exact diagonalization (ED) for a system size of 2^{10}. The left panels show the convergence error ϵ after ten rounds of SCF iterations as a function of various parameters: Panel (c) shows the error vs bond dimension χ for several values of Chebyshev polynomial order N_c; panel (d) shows the error vs N_c for several values of χ; panel (e) shows the error vs χ for different system sizes L; panel (f) shows the error vs χ for different KPM kernels. Calculations are performed on a one-dimensional super-moiré system, and comparisons with ED are done for a system size of 2^{10} sites, and we took $N_c = 250$ for panels (e) and (f). A total of $\mathcal{N} = 10$ iterations of the self-consistent loop are performed for solving the self-consistent tensor network equations for panels (a)–(f).

a certain χ and N_c, the self-consistent loop could be restarted with the converged solution using a higher value for χ and N_c. The approximate $\mathcal{O}(\log N)$ complexity directly leads to speedup of several orders of magnitude for system sizes above a million, making it possible to perform self-consistent calculations on systems with up to billions of sites, which were previously intractable. It is finally worth noting that the motivation for using tensor networks is not solely the reduction of computational time. Rather, the primary advantage lies in enabling calculations for extremely large systems where storing even a single sparse Hamiltonian matrix is infeasible due to memory constraints. By compressing the Hamiltonian into an MPO, we drastically reduce the memory cost and thus make it possible to store and manipulate the Hamiltonians at this scale.

For the accuracy benchmarking, as our algorithm fully relies on tensor networks, the bond dimension directly controls the fidelity of the MPO approximation. We took a bond dimension $\chi = 100$ for all calculations for one- and two-dimensional systems shown in the main text and Appendix. For one-dimensional systems, self-consistent errors were typically below 10^{-3}, while for the more challenging two-dimensional cases, errors remained within 2×10^{-3}, which are typical values of self-consistency error required to reach convergence in mean-field calculations in tight-binding models [98,99]. To further prove that a bond dimension of $\chi = 100$ ensures good precision in our calculations, we have benchmarked the performance of our method using one-dimensional super-moiré systems as in Fig. 9. Here, we analyze how the key parameters such as the bond dimension χ, the number of Chebyshev moments N_c, and the choice of KPM kernel influence the performance of the SCF calculations based on convergence error ϵ after $\mathcal{N} = 10$ rounds of iterations. First, we benchmark the accuracy of our method by directly comparing the results with those obtained via exact diagonalization (ED) for a large system. $N_c = 250$ is used for our algorithm. As shown in Fig. 9(b), the average deviation of electron densities between our tensor network approach and ED systematically decreases with increasing bond dimension χ as expected. Notably, the error drops below 10^{-3} for moderate bond dimensions, demonstrating that our method achieves very good quantitative agreement with ED. This

result confirms that our tensor network compression introduces only minimal approximation error when the bond dimension is chosen appropriately, validating the reliability of our approach for large-scale simulations. Furthermore, a plateauing behavior of the error curve appears with for increasing χ, especially when $\chi > 60$. Further increasing χ will not improve the precision, as in this region N_c is limiting the precision. This stems from the energy scale introduced by N_c, as $\delta_c \sim 1/N_c$ in the problem [71], similar to an effective smearing in the spectral functions, whose impact will be observed once the self-consistency error becomes comparable to or small than δ_c. Therefore, in order for KPM to agree with ED at those errors, a larger N_c will be needed.

For Figs. 9(c)–9(f), the left panels show the convergence error ϵ after $\mathcal{N} = 10$ SCF iterations as a function of various parameters, where for the nth iteration $\epsilon_n = |\rho_n - \rho_{n-1}|$, ρ_n being the electron densities at nth iteration. Figures 9(c) and 9(d) illustrate how χ and N_c affect the convergence behavior for a system with 2^{30} sites. Interestingly, we observe that when χ is small, increasing N_c leads to worse convergence [Fig. 9(d)], which can be rationalized as follows. If the number of polynomials N_c is increased to arbitrarily large values, the required bond dimension is likely to increase, in particular because the largest Chebyshev polynomial may require a large bond dimension to be properly captured. Specifically, an insufficient bond dimension gives rise to a reconstructed density of states that becomes negative at certain energies if N_c is too large. Therefore, the positivity of the density of states can be used as a proxy signaling that the bond dimension χ is large enough for a certain number of polynomials N_c. For sufficiently large χ, the convergence error can be made below a desired threshold for a wide range of number of polynomials N_c. These results highlight the importance of a balanced choice between N_c and χ: A high N_c is only beneficial when the bond dimension is large enough for the MPOs to correctly approximate the polynomial components, while larger χ will lead to heavy increase in computational time consumption. It finally worth noting that N_c controls the energy smearing in the calculation [100], analogous to temperature in experiments. As a result, very large N_c values are only necessary when resolving correlated states with very small energy scales. The interplay between N_c and χ will thus deserves a focused detailed study on its own, and we hope our findings will motivate further exploration in this direction.

Figure 9(e) presents the convergence error as a function of the bond dimension χ for systems of varying sizes and after $\mathcal{N} = 10$ iterations. The minimum error ϵ is thus bounded by the number of iterations $\mathcal{N}$. We solve our self-consistent tensor network problem with a linear mixing scheme, and therefore the self-consistency error reached after $\mathcal{N}$ iterations scales, in a best-case scenario, approximately as $\epsilon_{\mathcal{N}} = e^{-\lambda\mathcal{N}}$ [101], where λ depends on the mixing between new and old tensor networks. The number of iterations $\mathcal{N}$ was fixed at $\mathcal{N} = 10$ because this choice enables to reach errors below $\epsilon \equiv \epsilon_{\mathcal{N}=10} \sim 10^{-3}$ in our reference calculations. As a result, Fig. 9(e) highlights whether all different system sizes are able to reach convergence at a similar rate after $\mathcal{N} = 10$ iterations, and therefore enables quantifying if the finite bond dimension considered allows reaching a self-consistent solution after those iterations. As it is observed, all system sizes show a comparable convergence. It is also worth noting that for $L = 10$, bond dimension $\chi = 100$ corresponds to a fully covered Hilbert space, and therefore that calculation is equivalent to a full matrix implementation of the KPM self-consistent algorithm. As expected, at small χ, smaller systems exhibit lower errors than larger ones, consistent with their more compact representation. The key observation occurs at $\chi = 100$. Beyond this value $\chi = 100$, the convergence error becomes nearly system size independent, with exceptionally large systems achieving an accuracy comparable to small ones. This signifies that the tensor network has entered a regime where it faithfully represents the self-consistent solution. We note that more complex Hamiltonians may require a bigger bond dimension to reach the convergence level achieved in our calculations. An error ϵ below 10^{-3} at $\chi = 100$ is the typical value required for self-consistent studies of symmetry-broken states in graphene [98,99], and therefore it is fitting for our purposes. The fact that we achieve this precision self-consistently across system sizes up to a billion sites demonstrates that our chosen bond dimension is sufficient to reach a satisfactory convergence in our regime.

Finally, we compare the convergence performance of different kernel functions used in the KPM expansion [71]. Throughout this work, we primarily adopt the Jackson kernel [102], which effectively suppresses Gibbs oscillations arising from the Chebyshev truncation. It is defined as

$$g_n^J = \frac{(N_c - n + 1)\cos\left(\frac{n\pi}{N_c+1}\right) + \sin\left(\frac{n\pi}{N_c+1}\right)\cot\left(\frac{\pi}{N_c+1}\right)}{N_c + 1}. \quad \text{(E1)}$$

By applying g_n to nth Chebyshev polynomials $T_n(\mathcal{H})$, the Gibbs oscillations from truncation of KPM are suppressed. Although the Jackson kernel is the most popular choice in KPM calculations, to assess whether it still remains the optimal choice in the context of our methodology, we benchmark it against two widely used alternatives: the Fejér kernel

$$g_n^F = 1 - \frac{n}{N_c} \quad \text{(E2)}$$

and the Lorentz kernel

$$g_n^L = \frac{\sinh\left[\lambda\left(1 - \frac{n}{N_c}\right)\right]}{\sinh(\lambda)}, \quad \text{(E3)}$$

where λ is a parameter used for controlling the smoothness and we use $\lambda = 3$. As shown in Fig. 9(f), the Jackson kernel clearly outperforms the other two, providing the lowest convergence error across all settings. The Fejér kernel performs moderately well, while the Lorentz kernel exhibits the worst convergence, likely due to its limited ability to suppress high-order oscillations. This comparison confirms that the Jackson kernel remains the optimal choice for our approach for performing KPM calculations for tensor network compressed super-moiré Hamiltonians.

[1] J. M. Park, Y. Cao, K. Watanabe, T. Taniguchi, and P. Jarillo-Herrero, Tunable strongly coupled superconductivity in magic-angle twisted trilayer graphene, Nature (London) **590**, 249 (2021).

[2] X. Lu, P. Stepanov, W. Yang, M. Xie, M. A. Aamir, I. Das, C. Urgell, K. Watanabe, T. Taniguchi, G. Zhang, A. Bachtold, A. H. MacDonald, and D. K. Efetov, Superconductors, orbital magnets and correlated states in magic-angle bilayer graphene, Nature (London) **574**, 653 (2019).

[3] Y. Zhang, Z. Che, W. Liu, J. Wang, M. Zhao, F. Guan, X. Liu, L. Shi, and J. Zi, Unfolded band structures of photonic quasicrystals and moiré superlattices, Phys. Rev. B **105**, 165304 (2022).

[4] M. Yankowitz, S. Chen, H. Polshyn, Y. Zhang, K. Watanabe, T. Taniguchi, D. Graf, A. F. Young, and C. R. Dean, Tuning superconductivity in twisted bilayer graphene, Science **363**, 1059 (2019).

[5] A. Uri, S. C. de la Barrera, M. T. Randeria, D. Rodan-Legrain, T. Devakul, P. J. D. Crowley, N. Paul, K. Watanabe, T. Taniguchi, R. Lifshitz, L. Fu, R. C. Ashoori, and P. Jarillo-Herrero, Superconductivity and strong interactions in a tunable moiré quasicrystal, Nature (London) **620**, 762 (2023).

[6] D. R. Klein, L.-Q. Xia, D. MacNeill, K. Watanabe, T. Taniguchi, and P. Jarillo-Herrero, Electrical switching of a bistable moiré superconductor, Nat. Nanotechnol. **18**, 331 (2023).

[7] Y. Zeng, Z. Xia, K. Kang, J. Zhu, P. Knüppel, C. Vaswani, K. Watanabe, T. Taniguchi, K. F. Mak, and J. Shan, Thermodynamic evidence of fractional Chern insulator in moiré $MoTe_2$, Nature (London) **622**, 69 (2023).

[8] J. Cai, E. Anderson, C. Wang, X. Zhang, X. Liu, W. Holtzmann, Y. Zhang, F. Fan, T. Taniguchi, K. Watanabe, Y. Ran, T. Cao, L. Fu, D. Xiao, W. Yao, and X. Xu, Signatures of fractional quantum anomalous Hall states in twisted $MoTe_2$, Nature (London) **622**, 63 (2023).

[9] M. Serlin, C. L. Tschirhart, H. Polshyn, Y. Zhang, J. Zhu, K. Watanabe, T. Taniguchi, L. Balents, and A. F. Young, Intrinsic quantized anomalous Hall effect in a moiré heterostructure, Science **367**, 900 (2020).

[10] Z. Lu, T. Han, Y. Yao, A. P. Reddy, J. Yang, J. Seo, K. Watanabe, T. Taniguchi, L. Fu, and L. Ju, Fractional quantum anomalous Hall effect in multilayer graphene, Nature (London) **626**, 759 (2024).

[11] Y. Cao, V. Fatemi, A. Demir, S. Fang, S. L. Tomarken, J. Y. Luo, J. D. Sanchez-Yamagishi, K. Watanabe, T. Taniguchi, E. Kaxiras, R. C. Ashoori, and P. Jarillo-Herrero, Correlated insulator behaviour at half-filling in magic-angle graphene superlattices, Nature (London) **556**, 80 (2018).

[12] W. Zhao, B. Shen, Z. Tao, Z. Han, K. Kang, K. Watanabe, T. Taniguchi, K. F. Mak, and J. Shan, Gate-tunable heavy fermions in a moiré Kondo lattice, Nature (London) **616**, 61 (2023).

[13] H. Kim, Y. Choi, Lantagne-Hurtubise, C. Lewandowski, A. Thomson, L. Kong, H. Zhou, E. Baum, Y. Zhang, L. Holleis, K. Watanabe, T. Taniguchi, A. F. Young, J. Alicea, and S. Nadj-Perge, Imaging inter-valley coherent order in magic-angle twisted trilayer graphene, Nature (London) **623**, 942 (2023).

[14] V. Vaňo, M. Amini, S. C. Ganguli, G. Chen, J. L. Lado, S. Kezilebieke, and P. Liljeroth, Artificial heavy fermions in a van der Waals heterostructure, Nature (London) **599**, 582 (2021).

[15] E. Y. Andrei, D. K. Efetov, P. Jarillo-Herrero, A. H. MacDonald, K. F. Mak, T. Senthil, E. Tutuc, A. Yazdani, and A. F. Young, The marvels of moiré materials, Nat. Rev. Mater. **6**, 201 (2021).

[16] Q. Fu, P. Wang, C. Huang, Y. V. Kartashov, L. Torner, V. V. Konotop, and F. Ye, Optical soliton formation controlled by angle twisting in photonic moiré lattices, Nat. Photonics **14**, 663 (2020).

[17] L. Du, M. R. Molas, Z. Huang, G. Zhang, F. Wang, and Z. Sun, Moiré photonics and optoelectronics, Science **379**, 447 (2023).

[18] H. Tang, B. Lou, F. Du, M. Zhang, X. Ni, W. Xu, R. Jin, S. Fan, and E. Mazur, Experimental probe of twist angle-dependent band structure of on-chip optical bilayer photonic crystal, Sci. Adv. **9**, eadh8498 (2023).

[19] X.-R. Mao, Z.-K. Shao, H.-Y. Luan, S.-L. Wang, and R.-M. Ma, Magic-angle lasers in nanostructured moiré superlattice, Nat. Nanotechnol. **16**, 1099 (2021).

[20] A. A. Arkhipova, Y. V. Kartashov, S. K. Ivanov, S. A. Zhuravitskii, N. N. Skryabin, I. V. Dyakonov, A. A. Kalinkin, S. P. Kulik, V. O. Kompanets, S. V. Chekalin, F. Ye, V. V. Konotop, L. Torner, and V. N. Zadkov, Observation of linear and nonlinear light localization at the edges of moiré arrays, Phys. Rev. Lett. **130**, 083801 (2023).

[21] Y. V. Kartashov, F. Ye, V. V. Konotop, and L. Torner, Multifrequency solitons in commensurate-incommensurate photonic moiré lattices, Phys. Rev. Lett. **127**, 163902 (2021).

[22] H.-Y. Luan, Y.-H. Ouyang, Z.-W. Zhao, W.-Z. Mao, and R.-M. Ma, Reconfigurable moiré nanolaser arrays with phase synchronization, Nature (London) **624**, 282 (2023).

[23] A. González-Tudela and J. I. Cirac, Cold atoms in twisted-bilayer optical potentials, Phys. Rev. A **100**, 053604 (2019).

[24] T. Salamon, A. Celi, R. W. Chhajlany, I. Frérot, M. Lewenstein, L. Tarruell, and D. Rakshit, Simulating twistronics without a twist, Phys. Rev. Lett. **125**, 030504 (2020).

[25] J.-C. Yu, S. Bhave, L. Reeve, B. Song, and U. Schneider, Observing the two-dimensional Bose glass in an optical quasicrystal, Nature (London) **633**, 338 (2024).

[26] Z. Meng, L. Wang, W. Han, F. Liu, K. Wen, C. Gao, P. Wang, C. Chin, and J. Zhang, Atomic Bose-Einstein condensate in twisted-bilayer optical lattices, Nature (London) **615**, 231 (2023).

[27] L. A. Gonzalez-Arraga, J. L. Lado, F. Guinea, and P. San-Jose, Electrically controllable magnetism in twisted bilayer graphene, Phys. Rev. Lett. **119**, 107201 (2017).

[28] A. Ramires and J. L. Lado, Emulating heavy fermions in twisted trilayer graphene, Phys. Rev. Lett. **127**, 026401 (2021).

[29] A. Ferreira and E. R. Mucciolo, Critical delocalization of chiral zero energy modes in graphene, Phys. Rev. Lett. **115**, 106601 (2015).

[30] S. M. João, J. M. Viana Parente Lopes, and A. Ferreira, High-resolution real-space evaluation of the self-energy operator of disordered lattices: Gade singularity, spin–orbit effects and p-wave superconductivity, J. Phys. Mater. **5**, 045002 (2022).

[31] Y. Mao, D. Guerci, and C. Mora, Supermoiré low-energy effective theory of twisted trilayer graphene, Phys. Rev. B **107**, 125423 (2023).

[32] S. Carr, S. Fang, and E. Kaxiras, Electronic-structure methods for twisted moiré layers, Nat. Rev. Mater. **5**, 748 (2020).

[33] Y. Li, M. Xue, H. Fan, C.-F. Gao, Y. Shi, Y. Liu, K. Watanabe, T. Tanguchi, Y. Zhao, F. Wu, X. Wang, Y. Shi, W. Guo, Z. Zhang, Z. Fei, and J. Li, Symmetry breaking and anomalous conductivity in a double-moiré superlattice, Nano Lett. **22**, 6215 (2022).

[34] M. Kapfer *et al.*, Programming twist angle and strain profiles in 2D materials, Science **381**, 677 (2023).

[35] S. R. White, Density matrix formulation for quantum renormalization groups, Phys. Rev. Lett. **69**, 2863 (1992).

[36] U. Schollwöck, The density-matrix renormalization group, Rev. Mod. Phys. **77**, 259 (2005).

[37] U. Schollwöck, The density-matrix renormalization group in the age of matrix product states, Ann. Phys. **326**, 96 (2011).

[38] R. Orús, Tensor networks for complex quantum systems, Nat. Rev. Phys. **1**, 538 (2019).

[39] S. Yan, D. A. Huse, and S. R. White, Spin-liquid ground state of the $s = 1/2$ kagome Heisenberg antiferromagnet, Science **332**, 1173 (2011).

[40] Z. Zhu and S. R. White, Spin liquid phase of the $s = 1/2 j_1 - j_2$ Heisenberg model on the triangular lattice, Phys. Rev. B **92**, 041105(R) (2015).

[41] H. Xu, C.-M. Chung, M. Qin, U. Schollwöck, S. R. White, and S. Zhang, Coexistence of superconductivity with partially filled stripes in the Hubbard model, Science **384**, 202 (2024).

[42] H.-C. Jiang and T. P. Devereaux, Superconductivity in the doped Hubbard model and its interplay with next-nearest hopping t', Science **365**, 1424 (2019).

[43] R. Dilip, Y.-J. Liu, A. Smith, and F. Pollmann, Data compression for quantum machine learning, Phys. Rev. Res. **4**, 043007 (2022).

[44] Z.-Y. Han, J. Wang, H. Fan, L. Wang, and P. Zhang, Unsupervised generative modeling using matrix product states, Phys. Rev. X **8**, 031012 (2018).

[45] E. Stoudenmire and D. J. Schwab, Supervised learning with tensor networks, Adv. Neural Inf. Process. Syst. **29**, 4799 (2016).

[46] M. Niedermeier, J. L. Lado, and C. Flindt, Simulating the quantum Fourier transform, Grover's algorithm, and the quantum counting algorithm with limited entanglement using tensor networks, Phys. Rev. Res. **6**, 033325 (2024).

[47] Y. Zhou, E. M. Stoudenmire, and X. Waintal, What limits the simulation of quantum computers? Phys. Rev. X **10**, 041038 (2020).

[48] C. Huang *et al.*, Efficient parallelization of tensor network contraction for simulating quantum computation, Nat. Comput. Sci. **1**, 578 (2021).

[49] Y. N. Fernández, M. K. Ritter, M. Jeannin, J.-W. Li, T. Kloss, T. Louvet, S. Terasaki, O. Parcollet, J. von Delft, H. Shinaoka, and X. Waintal, Learning tensor networks with tensor cross interpolation: New algorithms and libraries, SciPost Phys. **18**, 104 (2025).

[50] M. K. Ritter, Y. Núñez Fernández, M. Wallerberger, J. von Delft, H. Shinaoka, and X. Waintal, Quantics tensor cross interpolation for high-resolution parsimonious representations of multivariate functions, Phys. Rev. Lett. **132**, 056501 (2024).

[51] H. Shinaoka, M. Wallerberger, Y. Murakami, K. Nogaki, R. Sakurai, P. Werner, and A. Kauch, Multiscale space-time ansatz for correlation functions of quantum systems based on quantics tensor trains, Phys. Rev. X **13**, 021015 (2023).

[52] A. Erpenbeck, W.-T. Lin, T. Blommel, L. Zhang, S. Iskakov, L. Bernheimer, Y. Núñez Fernández, G. Cohen, O. Parcollet, X. Waintal, and E. Gull, Tensor train continuous time solver for quantum impurity models, Phys. Rev. B **107**, 245135 (2023).

[53] Y. Núñez Fernández, M. Jeannin, P. T. Dumitrescu, T. Kloss, J. Kaye, O. Parcollet, and X. Waintal, Learning Feynman diagrams with tensor trains, Phys. Rev. X **12**, 041018 (2022).

[54] H. Takahashi, R. Sakurai, and H. Shinaoka, Compactness of quantics tensor train representations of local imaginary-time propagators, SciPost Phys. **18**, 007 (2025).

[55] M. Jeannin, Y. Núñez Fernández, T. Kloss, O. Parcollet, and X. Waintal, Cross-extrapolation reconstruction of low-rank functions and application to quantum many-body observables in the strong coupling regime, Phys. Rev. B **110**, 035124 (2024).

[56] N. Gourianov, M. Lubasch, S. Dolgov, Q. Y. van den Berg, H. Babaee, P. Givi, M. Kiffner, and D. Jaksch, A quantum-inspired approach to exploit turbulence structures, Nat. Comput. Sci. **2**, 30 (2022).

[57] R. D. Peddinti, S. Pisoni, A. Marini, P. Lott, H. Argentieri, E. Tiunov, and L. Aolita, Quantum-inspired framework for computational fluid dynamics, Commun. Phys. **7**, 135 (2024).

[58] N. Gourianov, P. Givi, D. Jaksch, and S. B. Pope, Tensor networks enable the calculation of turbulence probability distributions, Sci. Adv. **11**, eads5990 (2025).

[59] A. O. Fumega, M. Niedermeier, and J. L. Lado, Correlated states in super-moiré materials with a kernel polynomial quantics tensor cross interpolation algorithm, 2D Mater. **12**, 015018 (2025).

[60] M. Fishman, S. R. White, and E. M. Stoudenmire, The ITensor software library for tensor network calculations, SciPost Phys. Codebases 4 (2022).

[61] https://github.com/tensor4all/Quantics.jl.

[62] M. Ritter and contributors (2022), https://github.com/tensor4all/TensorCrossInterpolation.jl/tree/main.

[63] M. Ritter and contributors (2022), https://github.com/tensor4all/quanticstci.jl.

[64] T. Besard, C. Foket, and B. De Sutter, Effective extensible programming: Unleashing Julia on GPUs, IEEE Trans. Parallel Distrib. Syst. **30**, 827 (2019).

[65] T. Besard, V. Churavy, A. Edelman, and B. D. Sutter, Rapid software prototyping for heterogeneous and distributed platforms, Adv. Eng. Software **132**, 29 (2019).

[66] A. Holzner, A. Weichselbaum, I. P. McCulloch, U. Schollwöck, and J. von Delft, Chebyshev matrix product state approach for spectral functions, Phys. Rev. B **83**, 195115 (2011).

[67] J. L. Lado and O. Zilberberg, Topological spin excitations in Harper-Heisenberg spin chains, Phys. Rev. Res. **1**, 033009 (2019).

[68] G. Chen, F. Song, and J. L. Lado, Topological spin excitations in non-Hermitian spin chains with a generalized kernel polynomial algorithm, Phys. Rev. Lett. **130**, 100401 (2023).

[69] G. Chen, J. L. Lado, and F. Song, Many-body Liouvillian dynamics with a non-Hermitian tensor-network kernel polynomial algorithm, Phys. Rev. Res. **6**, 043182 (2024).

[70] T. V. C. Antão, Y. Sun, A. O. Fumega, and J. L. Lado, Tensor network method for real-space topology in quasicrystal Chern mosaics, arXiv:2506.05230.

[71] A. Weiße, G. Wellein, A. Alvermann, and H. Fehske, The kernel polynomial method, Rev. Mod. Phys. **78**, 275 (2006).

[72] The expansion in Eq. (5) can be formally applied with conventional sparse matrices H^{MF}; however, the full matrix with elements $\langle c_\alpha^\dagger c_\beta \rangle$ will be dense even when H^{MF} is sparse.

[73] I. Oseledets and E. Tyrtyshnikov, TT-cross approximation for multidimensional arrays, Linear Algebra Appl. **432**, 70 (2010).

[74] I. V. Oseledets, Tensor-train decomposition, SIAM J. Sci. Comput. **33**, 2295 (2011).

[75] P. Wang, Y. Zheng, X. Chen, C. Huang, Y. V. Kartashov, L. Torner, V. V. Konotop, and F. Ye, Localization and delocalization of light in photonic moiré lattices, Nature (London) **577**, 42 (2020).

[76] I. Caha, L. Boddapatti, A. ul Ahmad, M. Banobre, A. T. Costa, A. N. Enyashin, W. Li, P. Gargiani, M. Valvidares, J. Fernandez-Rossier, and F. L. Deepak, Magnetic single wall CrI_3 nanotubes encapsulated within multiwall carbon nanotubes, arXiv:2405.14967.

[77] D. Park *et al.*, Unconventional domain tessellations in moiré-of-moiré lattices, Nature (London) **641**, 896 (2025).

[78] Y. Ma, M. Huang, X. Zhang, W. Hu, Z. Zhou, K. Feng, W. Li, Y. Chen, C. Lou, W. Zhang, H. Ji, Y. Wang, Z. Wu, X. Cui, W. Yao, S. Yan, Z. Y. Meng, and N. Wang, Magnetic bloch states at integer flux quanta induced by super-moiré potential in graphene aligned with twisted boron nitride, Nat. Commun. **16**, 1860 (2025).

[79] M. Rösner and J. L. Lado, Inducing a many-body topological state of matter through Coulomb-engineered local interactions, Phys. Rev. Res. **3**, 013265 (2021).

[80] Z. Jiang, S. Haas, and M. Rösner, Plasmonic waveguides from Coulomb-engineered two-dimensional metals, 2D Mater. **8**, 035037 (2021).

[81] T. Tan, A. P. Reddy, L. Fu, and T. Devakul, Designing topology and fractionalization in narrow gap semiconductor films via electrostatic engineering, Phys. Rev. Lett. **133**, 206601 (2024).

[82] X. Lai, G. Li, A. M. Coe, J. H. Pixley, K. Watanabe, T. Taniguchi, and E. Y. Andrei, Moiré periodic and quasiperiodic crystals in heterostructures of twisted bilayer graphene on hexagonal boron nitride, Nat. Mater. **24**, 1019 (2025).

[83] C.-Y. Hao, Z. Zhan, P. A. Pantaleón, J.-Q. He, Y.-X. Zhao, K. Watanabe, T. Taniguchi, F. Guinea, and L. He, Robust flat bands in twisted trilayer graphene moiré quasicrystals, Nat. Commun. **15**, 8437 (2024).

[84] J. Haegeman, J. I. Cirac, T. J. Osborne, I. Pižorn, H. Verschelde, and F. Verstraete, Time-dependent variational principle for quantum lattices, Phys. Rev. Lett. **107**, 070601 (2011).

[85] S. Paeckel, T. Köhler, A. Swoboda, S. R. Manmana, U. Schollwöck, and C. Hubig, Time-evolution methods for matrix-product states, Ann. Phys. **411**, 167998 (2019).

[86] M. Niedermeier, A. Moulinas, T. Louvet, J. L. Lado, and X. Waintal, Solving the Gross-Pitaevskii equation on multiple different scales using the quantics tensor train representation, arXiv:2507.04262.

[87] A. Bou-Comas, M. Płodzień, L. Tagliacozzo, and J. J. García-Ripoll, Quantics tensor train for solving Gross-Pitaevskii equation, arXiv:2507.03134.

[88] Q.-C. Chen, I.-K. Liu, J.-W. Li, and C.-M. Chung, Solving the Gross-Pitaevskii equation with quantic tensor trains: Ground states and nonlinear dynamics, arXiv:2507.04279.

[89] J. Thijssen, *Computational Physics* (Cambridge University Press, 2007).

[90] C. Pisani, R. Dovesi, and C. Roetti, *Hartree-Fock Ab Initio Treatment of Crystalline Systems* (Springer Science & Business Media, Berlin, Heidelberg, 2012), Vol. 48.

[91] J. Enkovaara *et al.*, Electronic structure calculations with GPAW: A real-space implementation of the projector augmented-wave method, J. Phys.: Condens. Matter **22**, 253202 (2010).

[92] P. Haubenwallner and M. Heller, Fully numerical Hartree-Fock calculations for atoms and small molecules with quantized tensor trains, Electron. Struct. **7**, 025006 (2025).

[93] https://github.com/YITAOSUN42/SCF_with_MPO.

[94] N. Jolly, Y. N. Fernández, and X. Waintal, Tensorized orbitals for computational chemistry, Phys. Rev. B **111**, 245115 (2025).

[95] Y. Yang, S. Iblisdir, J. I. Cirac, and M. C. Bañuls, Probing thermalization through spectral analysis with matrix product operators, Phys. Rev. Lett. **124**, 100602 (2020).

[96] Q. Xu, N. Tancogne-Dejean, E. V. Boström, D. M. Kennes, M. Claassen, A. Rubio, and L. Xian, Engineering 2D square lattice Hubbard models in 90° twisted Ge/SnX (X = S, Se) moiré supperlattices, arXiv:2406.05626v1.

[97] P. Giannozzi Jr. *et al.*, Advanced capabilities for materials modelling with Quantum ESPRESSO, J. Phys.: Condens. Matter **29**, 465901 (2017).

[98] J. Fernández-Rossier and J. J. Palacios, Magnetism in graphene nanoislands, Phys. Rev. Lett. **99**, 177204 (2007).

[99] O. V. Yazyev, Emergence of magnetism in graphene materials and nanostructures, Rep. Prog. Phys. **73**, 056501 (2010).

[100] T. M. Radchenko, A. A. Shylau, I. V. Zozoulenko, and A. Ferreira, Effect of charged line defects on conductivity in graphene: Numerical Kubo and analytical Boltzmann approaches, Phys. Rev. B **87**, 195448 (2013).

[101] G. Kresse and J. Furthmüller, Efficient iterative schemes for *ab initio* total-energy calculations using a plane-wave basis set, Phys. Rev. B **54**, 11169 (1996).

[102] D. Jackson, On approximation by trigonometric sums and polynomials, Trans. Am. Math. Soc. **13**, 491 (1912).